



## **Final Draft of the original manuscript**

Landell, R.; de Lima Lessa, C.; Bergmann, L.; dos Santos, J.;  
Kwietniewski, C.; Klusemann, B.:

**Investigation of friction stir welding process applied to ASTM  
572 steel plate clad with Inconel®625.**

In: Welding in the World. Vol. 65 (2021) 393 - 403.

First published online by Springer: 16.11.2020

<https://dx.doi.org/10.1007/s40194-020-01007-w>

# Investigation of friction stir welding process applied to ASTM 572 steel plate clad with Inconel® 625

Renan Mensch Landell<sup>1,2</sup> · Cleber Rodrigo de Lima Lessa<sup>1,3</sup> · Luciano Bergmann<sup>1</sup> · Jorge Fernandez dos Santos<sup>1</sup> · Carlos Eduardo Fortis Kwietniewski<sup>2</sup> · Benjamin Klusemann<sup>1,4</sup>

This study investigates friction stir welding (FSW) in the dissimilar joining process of clad plates. Samples of 4-mm thick ASTM 572 steel plate clad with 3-mm thick Inconel®625 represent the base material. In order to limit mixing between the dissimilar materials to keep the corrosion resistance, a two-pass welding procedure was applied. Optimal welding parameters for each pass were identified. The welded specimens were evaluated by light microscopy, SEM equipped with EDS, and mechanical tests such as hardness, bending, and tensile testing. Defect-free joints with excellent surface finish have been obtained with a well-defined interfacial region between both materials. The FSW process changed the microstructure of both metals used in this study to a new refined grain region into the weld with complex microstructure inside the ASTM 572 steel, as well as change from a dendritic to an equiaxial microstructure in the Inconel®625. The breaking and the distribution of the intermetallic and secondary phases of the nickel alloy were promoted by the FSW process, moreover the second welding pass on the Inconel® tempered the steel which had previously been welded in the first FSW weld pass. The mechanical properties within the welding zone increased due to this microstructural rearrangement coupled with the Hall-Petch effect.

## 1 Introduction

Inconel®625 is a nickel-based superalloy with face-centered cubic (fcc)  $\gamma$ -phase matrix, mainly strengthened by solid solution of chromium, molybdenum, and niobium elements as well as by the formation of intermetallic and secondary phases [1, 2]. The material presents excellent corrosion, thermal-fatigue, and

creep resistance properties which allow the use of the alloy in severe operation conditions, as present for the oil and gas, chemical, and aerospace industries [3, 4]. The addition of Cr provides the formation of a protective oxide layer ( $\text{Cr}_2\text{O}_3$ ) at the surface, and the Mo content improves the localized corrosion resistance against pitting and crevice corrosion [5, 6]. In the oil and gas industry, Inconel®625 is normally used as corrosion resistant alloy (CRA) in the interior of carbon steel pipes and pressure vessels due to the high aggressiveness of the crude oil, where the presence of organic acids, hydrogen sulfide, sand, carbon dioxide, and active chloride limit the use of low alloyed steels [1, 2, 7, 8]. Despite its property advantages, the use of nickel-based alloys as clad material brings big challenges for the joining process due to the high dissimilarity of the carbon steel pipe and the internal CRA layer. This high level of material heterogeneity can lead to detrimental secondary phases and intermetallic formation in the girth welds [4, 9].

Conventional arc-welding processes applied to the joining of clad pipes normally use a filler material with the same or overmatching corrosion resistance by featuring a chemical composition equal or higher than the CRA to guarantee the corrosion resistance. But the addition of material does not

✉ Cleber Rodrigo de Lima Lessa  
cleber.r.lessa@gmail.com

<sup>1</sup> Helmholtz Zentrum Geesthacht, Institute of Materials Research, Materials Mechanics, Solid State Joining Processes (WMP), Max Planck Straße 1, Geesthacht 21502, Germany

<sup>2</sup> Physical Metallurgy Laboratory (LAMEF) PPGE3M/UFRGS, Av. Osvaldo Aranha 99 s.610, 90035 190 Porto Alegre, Brazil

<sup>3</sup> Federal Institute of Rio Grande do Sul (IFRS), R. Avelino Antônio de Souza 1730, 95043 700 Caxias do Sul, Brazil

<sup>4</sup> Institute of Product and Process Innovation, Leuphana University of Lüneburg, Universitätsallee 1, Lüneburg 21335, Germany

avoid issues related to the dilution of the base metal inside the weld, dendritic microstructures in the girth weld, differences in fluidity, and melting temperature of both joining partners and the high energy input in the substrate that can lead to lack of fusion, hard interfacial regions, solidification cracking, and diffusion issues [1, 10–12]. Xu et al. [13] mentioned that the corrosion passivation current density ( $I_{\text{corr}}$ ) of root arc welds is the most negative one to pitting corrosion. Besides that, during the solidification of the weld metal, segregation of elements such Cr, Mo, and Nb into the grain boundaries promotes the formation of intermetallic, carbides, and topologically closed-packed (TCP) phases like Laves, P-phase,  $\mu$ -phase, and  $\sigma$ -phase. The presence of these phases reduces the corrosion resistance of the dendritic core due to the depletion of these elements. Additionally, mechanical properties of the weld can be affected by the distribution and size of the intermetallic and secondary phases [14–16]. Therefore, several authors described that to control the detrimental effects of the segregates, like the Laves phase, the size and distribution in the matrix must be reduced by altering the welding energy input, the application of post weld heat treatments, and increasing the cooling rate of the weld [17–19].

Thus, the application of a new joining process that reduces the complexity of welding those dissimilar materials is aimed by the industry. Friction stir welding (FSW) has gained increasing interest since its invention at TWI and has already proved to be an outstanding joining process for dissimilar material combinations, including aluminum to steel [20, 21], aluminum to nickel [22], aluminum to titanium [23, 24], magnesium to steel [25], and other combinations [26, 27]. However, the joining of plates consisting of carbon steel and a nickel alloy as clad is a novelty in the FSW literature. Due to the high plasticizing temperature and high mechanical resistance of these two materials, studies on FSW of each one of them alone are also rare; however, the so far available studies reported good results for FSW of nickel-based alloys and carbon steels [2, 3]. Low rotational speeds and high forces are reported to lead to better mechanical and corrosion properties of the nickel weld [2, 3].

In the present study, the feasibility of FSW to the joining of ASTM 572 steel plates clad with Inconel®625 is presented. A two-pass welding procedure is proposed to join the plates. Mechanical and microstructural evaluations were performed by several experimental techniques, highlighted in the following.

## 2 Experimental procedure

### 2.1 Material selection and process parameters

In order to obtain the clad base material (BM) required for this study, the following procedure was carried out. An ASTM 572 Gr. 50 steel plate with 19.05 mm of thickness and

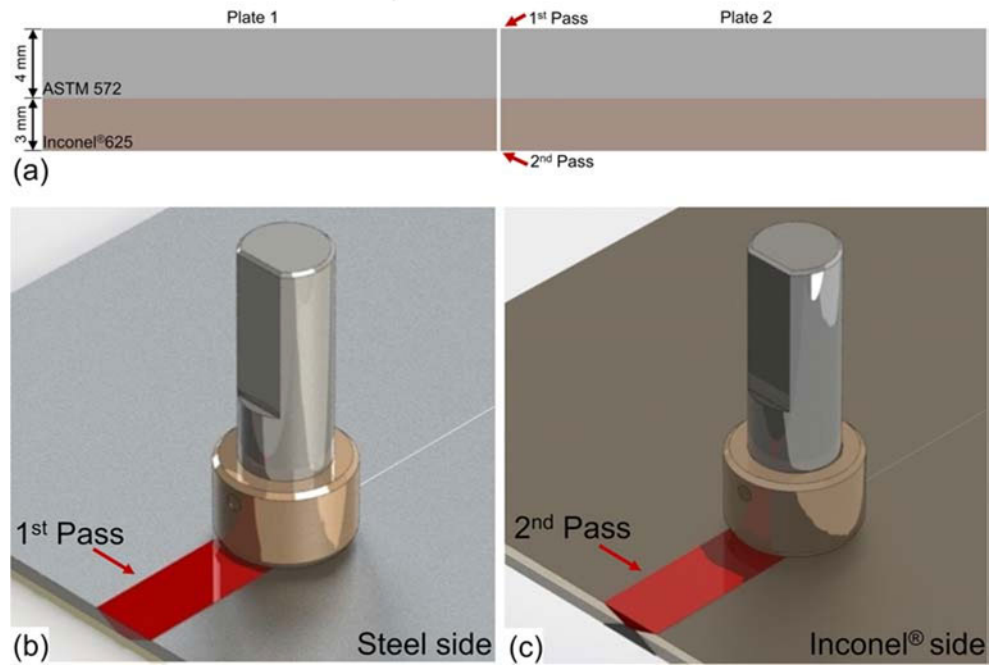
500 mm × 500 mm was coated by a gas tungsten arc welding (GTAW) process. The AWS ER NiCrMo-3 filler material was used to produce the Inconel®625 coating with two layer deposition, i.e., 1st layer, which is closer to the ASTM 572 and the 2nd layer on top of the 1st layer. It is important to use two or more layer of the CRA to reduce the amount of diluted Fe from the steel substrate into the Inconel®625 deposition, to improve the overall corrosion resistance properties [28]. Besides that, high Fe concentration changes the segregation potential of the alloy elements during the solidification of the nickel alloy [29, 30]. A post weld heat treatment to relief the plate stress was performed at 630 °C for 1 h after the Inconel®625 deposition. After that, six samples of 150 mm width, 500 mm length, and 7 mm thickness were prepared to enable three different welds. The final thickness of the base material (BM) to be used in the FSW process was 7 mm, consisting out of 3 mm out of Inconel®625 and 4 mm of ASTM 572 steel (Fig. 1a). The chemical composition of the steel plates and the Inconel®625 coating material are summarized in Table 1.

A butt weld joint configuration (Fig. 1a), with a two-pass welding procedure, is used to reduce the mixture between the two different materials during joining the clad plates. The welding procedure started with the welding of the steel side (1st pass), and then the plate was flipped upside down, and the nickel alloy side was welded (2nd pass); see Fig. 1b–c. Specific polycrystalline cubic boron nitride (PCBN) tools Q70, with 30% of Re as binder material, with probe lengths of 3 and 4 mm to weld the nickel and steel side, respectively, were used for each pass of the welding procedure. A total of three specimens were welded by FSW using six plates. The tool tilt angle was 0.5°, and argon as shielding gas was applied to all samples in order to avoid superficial material oxidation. Table 2 summarized the parameters used for each material side, that is, the 1st and 2nd welding pass, and the calculated energy input based on the parameters and machine torque during the welding [31] is given for completeness. A low-energy input (under 2.30 kJ/mm) is important to guarantee sound joints, which are free of porosity, in particular in Inconel®625 [32].

### 2.2 Microstructure and mechanical characterization

The light optical microscopy Keyence VHX-6000 (OM) and the scanning electron microscope Quant 650 FEG (SEM), equipped with energy-dispersive spectroscopy (EDS), were used to analyze the microstructure. The SEM was used in particular to identify and evaluate possible secondary phases such carbides and intermetallic in the nickel alloy. The cross-sectional areas were grounded, polished, and chemically etched using standard metallographic techniques. Adler and Nital 2% etching solutions were used to reveal the microstructure of the nickel alloy and the steel, respectively.

**Fig. 1** A two pass welding procedure is applied to reduce the mixture of the steel and Inconel®625 material. **a** Schematic showing a butt weld joint configuration with two plates. **b** First, the steel ASTM 572 and **(c)** second the Inconel®625 part are welded



In addition to the microstructural and metallurgical characterization, mechanical evaluations were done via Vickers hardness mapping, bending, and tensile testing to assess the mechanical properties of the joint. Vickers hardness maps of the welds were carried out on cross-sections of the weld with a Struers DuraScan 70 machine, using 500 g load (HV 0.5) and 0.5-mm indentation distance to verify the hardness distribution. Bending tests of each side of the weld were done following the ASME BPVC.IX standard, performed in a manual 200 kN hydraulic press. Tensile test specimens over the full thickness were machined and tested according to the DIN EN ISO 4136: 2011-05 [33] to determine the transverse tensile properties of the welded materials. The weld is located within the center of the gauge section. At total, nine tensile samples were machined, three from each specimen.

### 3 Results and discussions

#### 3.1 Macrostructure and microstructure observation

The base material microstructure of ASTM 572 steel and Inconel®625 clad layers, before to FSW, is presented in

Fig. 2. Both Inconel®625 layers present a columnar dendritic microstructure resulted from the Inconel®625 GTAW coating solidification; see also Fig. 3. Comparing the two layers, the 1st had smaller dendrites due the nucleation rate that was higher than the growth rate during the solidification [34]. The ASTM 572 presents two distinct microstructure regions, one heat-affected zone (HAZ) next to the clad deposition layer, composed mainly of bainite (B), but also acicular ferrite (AF) and Widmanstätten ferrite (W), see Fig.2c, and the base material with well-defined banded perlite (P) and ferrite (F) structures oriented according to the rolling direction; see Fig. 2d.

A detailed investigation via SEM and EDS for the Inconel®625 is presented in Fig. 3. The micrographs show the presence of intermetallic and secondary phases accumulated in the interdendritic region of the Ni-fcc matrix. The 1st layer, deposited over the steel substrate, formed more intermetallic and secondary phases which are bigger than the ones formed in the 2nd layer. This behavior might be related with the higher dilution of the steel elements inside the first CRA layer and with the energy input added by the deposition of the 2nd clad layer. During the solidification of the Inconel®625, elements such as Nb and Mo are segregated into the interdendritic region, and this enrichment of element concentration increases the number

**Table 1** Chemical composition (wt.%) of the Inconel®625 coating wire and ASTM 572 Gr. 50 substrate

Alloy	Elements (wt.%)												
	Ni	C	Cr	Mo	Nb	Fe	Cu	Ti	Si	Ta	P	S	Al
Inconel®625 coating wire	65.1	0.006	21.81	8.63	3.48	0.44	0.2	0.17	0.04	0.05	0.007		0.15
ASTM 572 steel		0.23				Bal.			0.40		0.04	0.05	

**Table 2** Welding parameters employed in this study for the three different samples

Specimens	Welding Pass	Rotational Speed [rpm]	Welding Speed [mm/s]	Force [kN]	Energy Input [kJ/mm]
A	1st pass (ASTM 572)	400	4	40	1.20
	2nd pass (Inconel@625)	250	2	60	1.30
B	1st pass (ASTM 572)	400	6	40	0.90
	2nd pass (Inconel@625)	300	2	60	1.33
C	1st pass (ASTM 572)	400	8	40	0.51
	2nd pass (Inconel@625)	200	2	60	1.05

The energy input is calculated according to [31]

intermetallic and of secondary phases [35]. Furthermore, the EDS chemical analysis results indicate that a higher amount of Fe is diluted in the 1st layer of Inconel@625, that is, 25.02% in weight than in the 2nd layer, i.e., 6.60 wt.% Fe, as shown in Fig. 3 b and d. Besides that, as can be seen from the EDS results in Fig. 4, most of the intermetallic and of secondary phases found are Laves and Nb-rich MC carbides. According to DuPont et al. [1] and Song and Nakata [2], both Laves and Nb-rich MC carbides are common in Fe-Ni alloys. Laves normally appear during the material solidification or during high-

temperature exposition and are characterized by large intergranular particles as seen in Fig. 4b.

Figure 5 shows the macrographs of the produced joints by FSW process for specimens A(a), B(b) and C(c). The resulting weld formation on the Inconel@ side (upper part) and the ASTM 572 steel side (bottom part) due to the two-pass welding process is clearly visible. The welds present a good finishing with no visual defects. In the Inconel@625 joint part, the microstructure appears more homogenous, and the dendritic morphology is no longer present. In addition, due to the

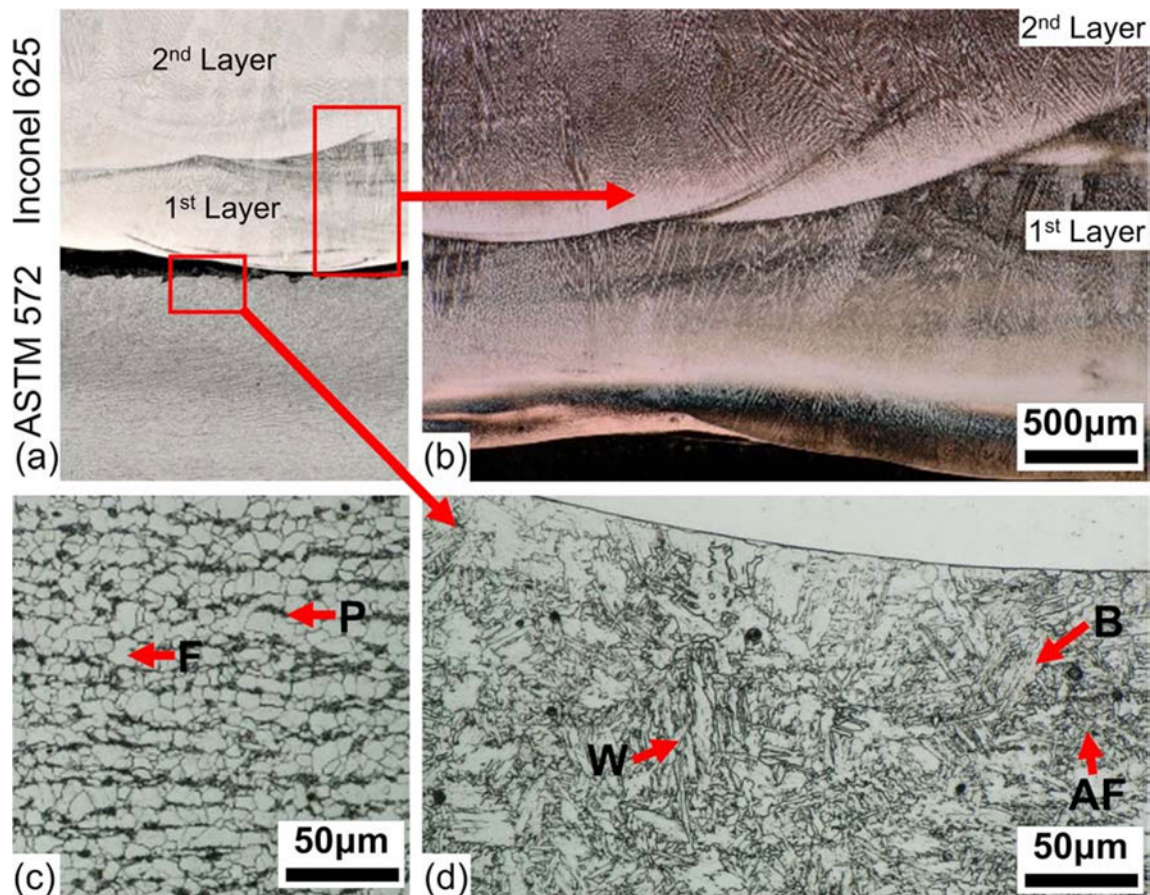


**Fig. 2** a Optical macrographs showing Inconel@625 coating, consisting of two layers and ASTM 572 base metal. b 1st layer and 2nd layer of Inconel@625 that present a columnar dendritic microstructure. c ASTM

572 base material showing banded perlite (P) and ferrite (F). (d) HAZ ASTM 572 showing bainite (B), but also acicular ferrite (AF) and Widmanstätten ferrite (W)

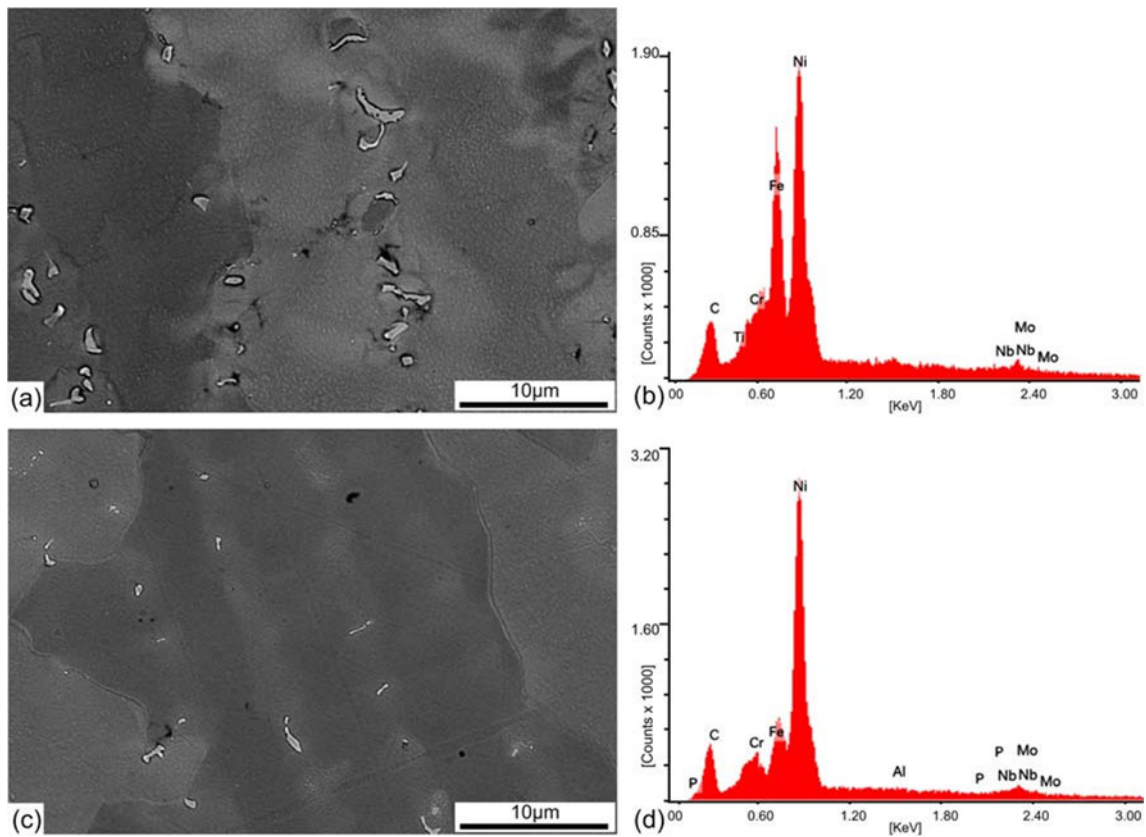


Fig. 3 Representative microstructures of the Inconel@625 in (a) 1st layer and (c) 2nd layer including the corresponding EDS chemical analysis results (b, d)

applied Adler etching solution, the clad layer boundaries are revealed, and the existing fusion line due to the GTAW process, used to produce the Inconel@625 coating between the steel and the Inconel@625, is over etched.

Analyzing the welds at the Inconel@625 side, it is possible to verify that there is almost no mixture between the dissimilar materials. While specimens A and C present a small mixture of the materials in the weld interface, specimen B shows more material mixture in this region, and thin layers of steel have been brought into the clad layer during the FSW process. There is no clear evidence that the differences of the material

mixture of the welds are specific related to the welding parameters, but the thickness relation, 4 mm for ASTM572 and 3 mm for the Inconel@625, could not be kept fully constant during machining the plates, and the differences of the welding parameters might allow the tool to touch the steel during welding of the Inconel@. Although the mixture might slightly differ, the results show that all samples followed a similar pattern of material flow in the stir zones of the nickel alloy.

As can be seen in Fig. 5 and Table 2, the HAZ size on the steel side is directly related with the energy input introduced in the first welding pass, i.e., the highest energy input led to the

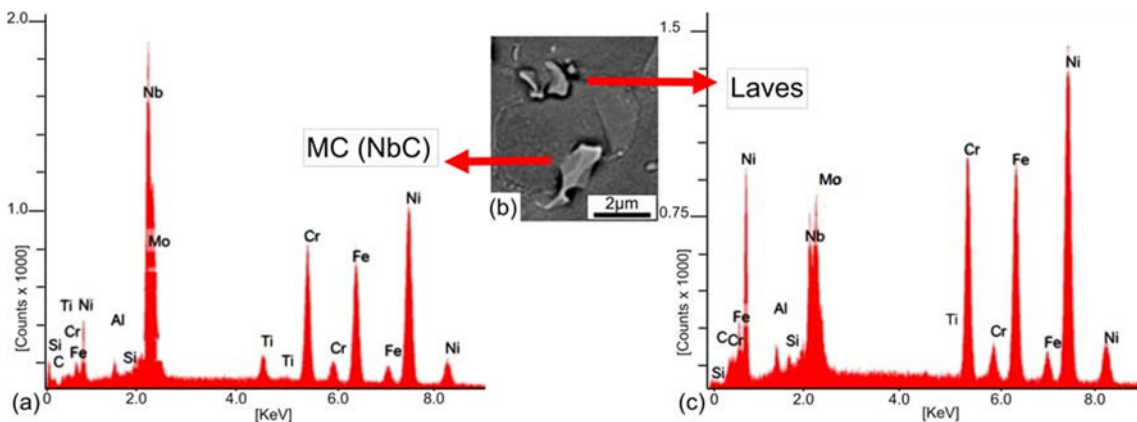


Fig. 4 a EDS pattern of MC (NbC) carbides, b representative microstructure of Laves and MC (NbC), and (c) EDS pattern of Laves

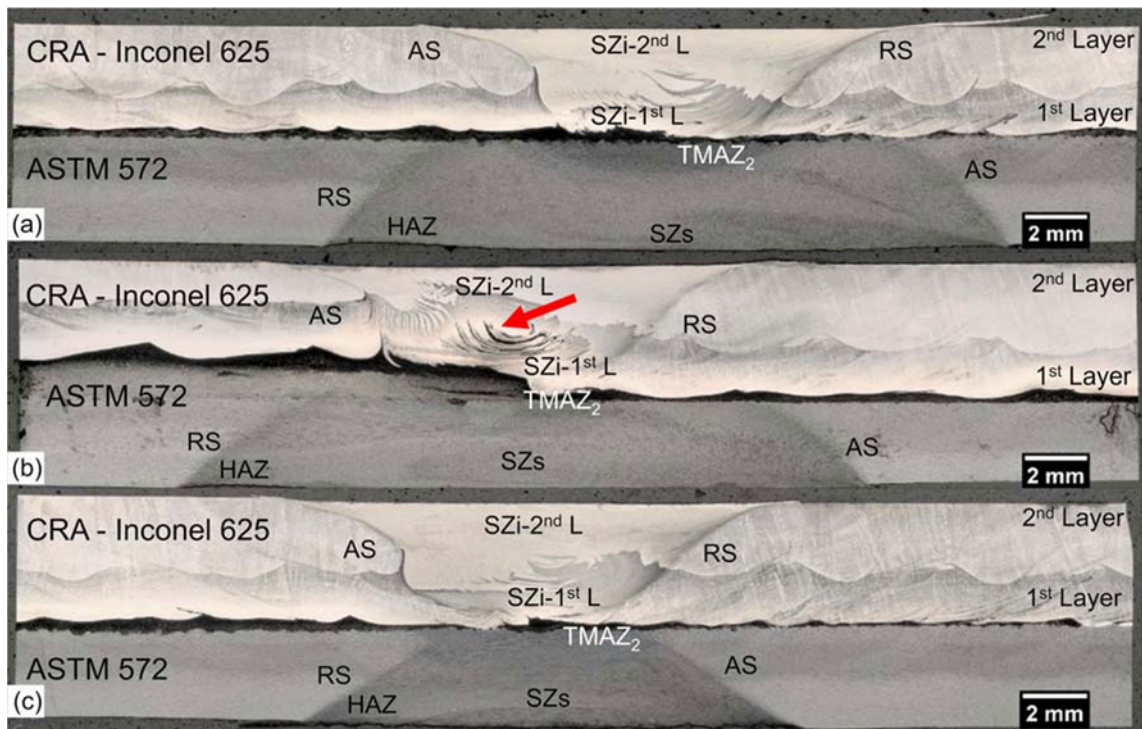


Fig. 5 Cross sectional macrograph of welds for specimens (a) A, (b) B, and (c) C

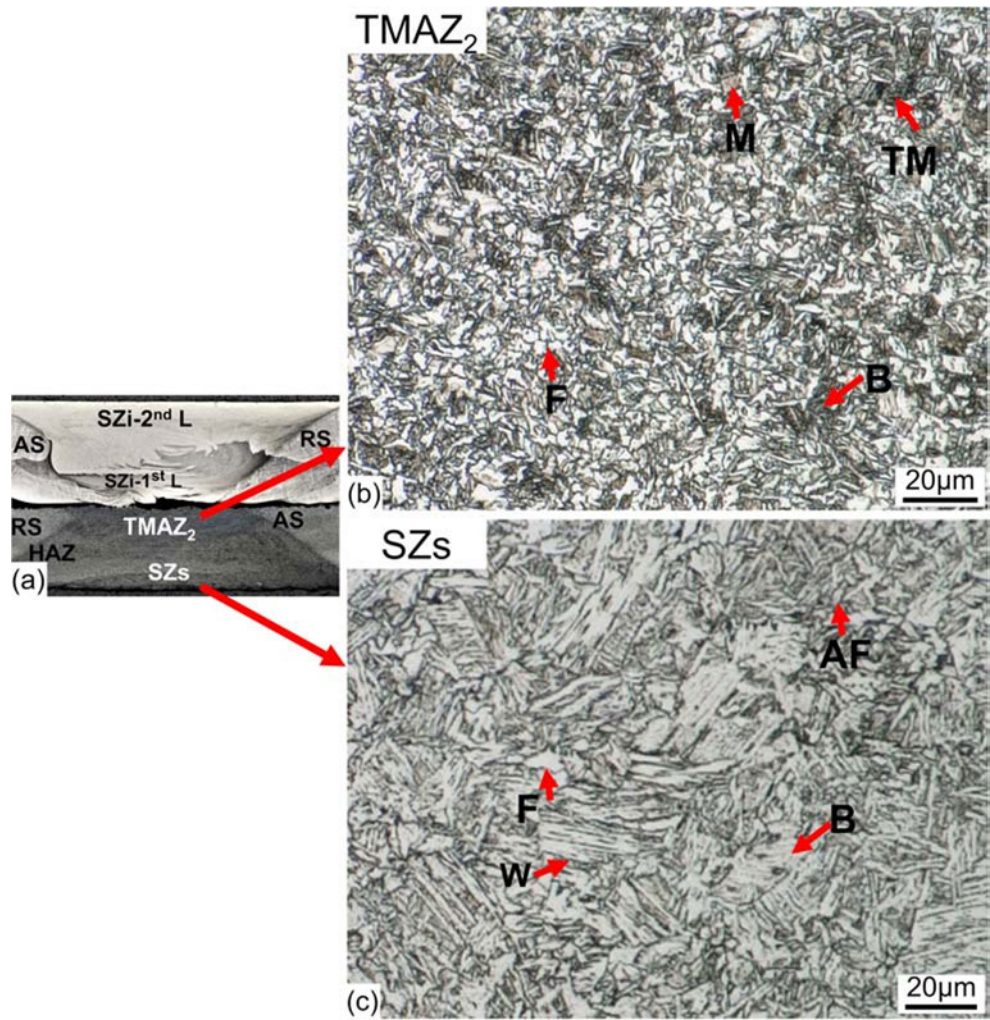
largest HAZ. The Inconel®625 was etched by the Adler solution that revealed the clad layers boundaries, resulting in the fact that the 1st layer is darker than the 2nd layer due to the difference in Fe dissolution. The ASTM 572 steel was etched by Nital 2% that revealed a second thermo-mechanically affected zone (TMAZ<sub>2</sub>) inside the steel welds, and next to the weld interface, it is assumed that this region resulted from the energy input from the 2nd welding pass (Inconel®625). This area shows a geometry similar to the tool probe. The arrow shows the thin layers of steel that have been brought into the clad layer during the FSW process. The black line crossing the center is the steel material that has been over etched by the Adler solution.

The final microstructures of the stir zone and the TMAZ<sub>2</sub> in the ASTM 572 weld are shown in Fig. 6, presenting a complex multiphase microstructure mainly composed by ferrite (F), acicular ferrite (AF), bainite (B), tempered martensite (TM), and martensite (M). Similar results were obtained by other authors [31, 36] during the welding of carbon steels with FSW, and they found that the presence of different morphologies within the microstructure connected with a suitable grain refinement ensured a balance between strength and toughness. Comparing the microstructures in both zones, it is possible to verify that the grains located in the SZs are larger and coarser. This microstructure differences might be related to the second welding pass, once the energy input was not enough to overcome the austenitization temperature but enough to make the steel tempering in the stir zone near to SZi 1st layer. As the TMAZ<sub>2</sub> is closer to the Inconel® weld,

higher temperatures were reached during the 2nd welding pass, enough to promote recrystallization of the material. This effect is clearly presented on the hardness map analysis; see Fig. 8.

Representative micrograph from Fig. 6a of the stir zone microstructures at the bottom (1st layer) and at the top (2nd layer) of the Inconel®625 is shown in Fig. 7. The micrographs show the change of the dendritic microstructure to a refined equiaxed Ni-fcc grain structure with twin grains due to the dynamic recrystallization imposed by the thermo-mechanical process [3]. Besides that, size reduction was obtained of the grain, of the intermetallics, and of the secondary phase as well. Before the FSW process, the average of secondary phases size was 1.35 μm and 0.93 μm in the 1st and 2nd layers of the Inconel®625 coating, respectively. After the FSW process, the average size of intermetallics and the secondary phases, that is, carbides and Laves, changed to 0.93 μm and 0.58 μm, respectively, representing a reduction of more than 30%. Moreover, the carbides and Laves were redistributed inside the weld. Following the same pattern of the base material, Fig. 3, the microstructure close to the steel substrate, i.e., 1st layer, presented more intermetallic phases than in the stir zone at the top of the weld. The intermetallics are mostly localized in the grain boundaries, but small round intermetallics are distributed inside of some grains, i.e., the results indicate that the FSW process promoted the break and the distribution of intermetallics and the secondary phases, which in theory tends to improve the mechanical properties of the material [37].

**Fig. 6** (a) Macrostructure showing the different welding zones: stir zone of the Inconel®625 (SZi), stir zone of ASTM 572 steel (SZs), thermo mechanically affected zone (TMAZ<sub>2</sub>), and heat affected zone (HAZ). (b) Final microstructure in the TMAZ<sub>2</sub> showing martensite (M), tempered martensite (TM), bainite (B), and ferrite (F). (c) SZs showing bainite (B), acicular ferrite (AF), Widmanstätten ferrite (W), and ferrite (F). Retreating side (RS) and advancing side (AS) are indicated

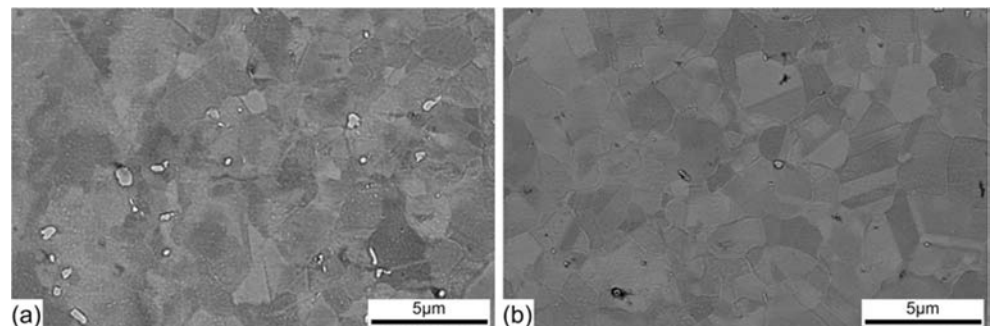


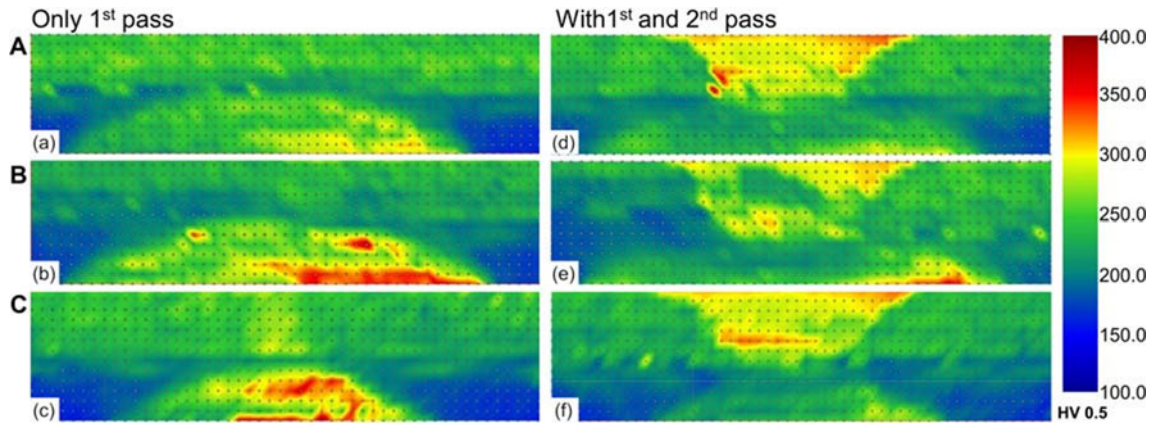
### 3.2 Hardness tests

Figure 8 depicts the hardness distribution along the cross-section of the welds along the thickness of the specimens A, B, and C. Before the welding, the Inconel®625 base material has an average hardness value around 250 HV 0.5, while the ASTM 572 base material exhibits an average hardness of 150 HV 0.5. Hardness maps after the 1st FSW welding pass in the ASTM 572 are shown, Fig. 8a–c, as well as after the 2nd

FSW welding pass in Inconel®625, Fig. 8d–f. The average hardness values increased in the stir zone and in the heat-affected zone of both materials due to microstructural transformations as well as the Hall-Petch effect [3, 7]. After the 1st pass on the ASTM 572, the three specimens showed the same behavior in the hardness distribution on the retreating side (RS) and advancing side (AS). There are lower hardness values in RS, approximately 250 HV 0.5; on the other hand, higher hardness values are mainly present in the top of the AS,

**Fig. 7** SEM micrographs showing the Inconel® matrix with intermetallics and secondary phases in the stir zone of the weld. (a) Micrograph of the bottom 1st layer and (b) of the 2nd layer in top of the Inconel® coating after FSW





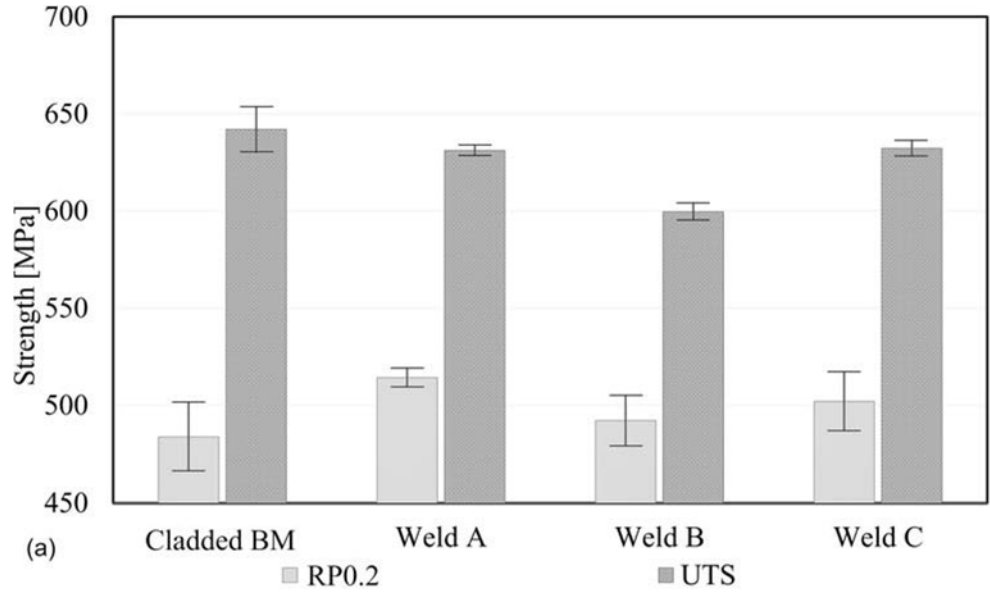
**Fig. 8** Hardness map after 1st welding pass in the specimens (a) A, (b) B, and (c) C. Hardness map after 1st and 2nd welding pass in the specimens (d) A, (e) B, and (f) C. The Inconel@625 nickel alloy is present at the top and the ASTM 572 steel at the bottom

about 350 HV 0.5. However, a depletion of the hardness in the ASTM 572 steel weld, to a hardness between 200 and 250 HV 0.5, is present after the 2nd welding pass, which is probably due to the higher energy input; see Table 2. This change is clear in the center of the stir zone and under the TMAZ<sub>2</sub> and corroborates with the microstructure changes found before, i.e., the tempered martensite in Fig. 6b. Meanwhile, in the Inconel@625 side, the weld leads to an average hardness close to 300 HV 0.5, with small diffuse areas with even higher but also lower hardness values.

### 3.3 Tensile and bending tests

Figure 9a presents the average ultimate tensile strength (UTS) and the yield strength (RP0.2) for the cladded BM and the different welds. According to the ASTM A572/A572M – 18 standard, the UTS and RP0.2 for the ASTM 572 steel are 450 MPa and 345 MPa, respectively. For the Inconel@625, the AWS ER NiCrMo-3 standard, the UTS and RP0.2 are 770 MPa and 510 MPa, respectively. The tensile results are showing that the cladded BM reached a UTS of  $642 \pm 12$  MPa

**Fig. 9** (a) Tensile test results obtained for the cladded base material as well as welded specimens. (b) Tensile specimen showing failure outside of the FSW region



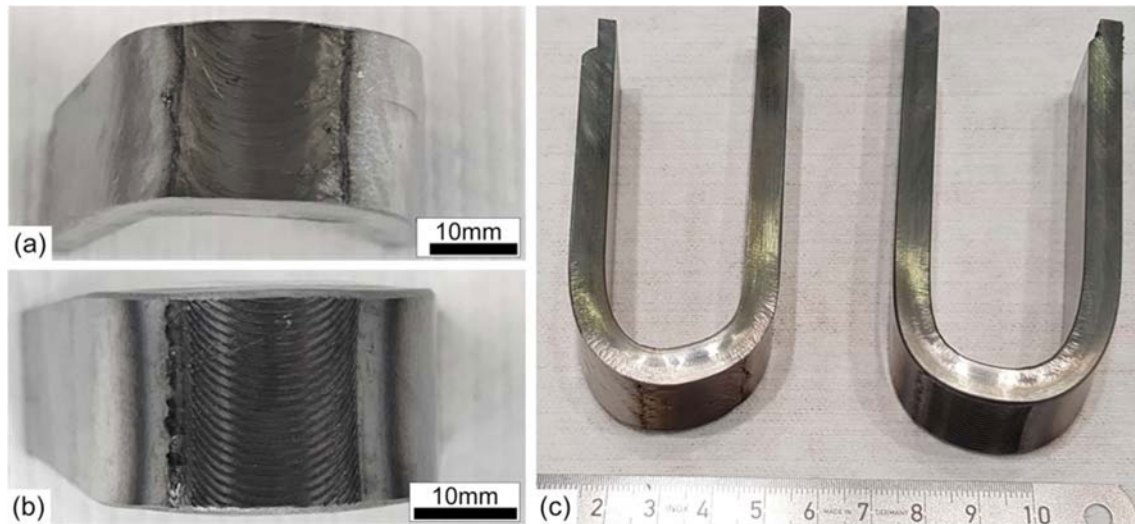


**Fig. 10** Bending test of different C specimens: (a) Inconel@625 weld bended surface. (b) ASTM 572 weld bended surface. (c) Final angle reached at ASTM 572 direction. (d) Final angle reached at Inconel@625 direction

and the welded specimens reached a similar UTS, as reason that the failure of the welded samples occurred in the clad BM; see Fig. 9b. This indicates improved mechanical properties of the weld region due to grain refinement, microstructural changes, and the break and distribution of the intermetallics and the secondary phases [37].

According to the ASME BPVC.IX standard, the acceptable limit size for discontinuities on the convex part of the specimen during the bend test as well as after the test is less than 1.5 mm to the clad material and 3.0 mm to the substrate. The measured bend angles after the test were 180 degrees to both Inconel@625 and to ASTM 572, and there were no discontinuities in the welded joints. Figure 10 presents the bended specimens of specimen C, as a representative result of the other specimens, once the samples A and B showed similar results. Figure 10 a and b illustrate the bended surfaces of the nickel and steel weld, while Fig. 10 c and d present the final angle of the specimens.

## 4 Conclusions

The joining of plates consisting of carbon steel and a nickel alloy as clad is a novelty in the FSW literature. Microstructural characterization and mechanical tests have been conducted on friction stir welded ASTM 572 Gr.50 steel plate, clad with Inconel@625. A two-pass welding procedure has been successfully demonstrated to produce defect free joints, starting with the welding of the steel side followed by welding of the Inconel 625 side. The main conclusions are summarized as follows:

1. The FSW process changed the microstructure of the Inconel@625 and the ASTM 572 steel, where a new

refined grain region into both stir zones was obtained. A complex microstructure composed by Widmanstätten ferrite, acicular ferrite, bainite, and ferrite was found inside the steel stir welding zone. The FSW process imposed a change from a dendritic to an equiaxial microstructure in the Inconel@625.

2. As expected, due to the energy input during the cladding process, most of the secondary phases and precipitates found are Laves and Nb-rich MC carbides. The FSW promoted the break and the distribution of these intermetallic and secondary phases in the Inconel@625. On the steel side, the HAZ size is directly related to the energy input introduced during the 1st welding pass.
3. The hardness of the materials increased inside both welds, but the energy input of the 2nd welding pass reduced the hardness in the steel compared with the value after the 1st welding pass. Besides that, the energy input from the 2nd welding pass generates a second thermo-mechanically affected zone (TMAZ<sub>2</sub>) inside the steel with a complex multiphase microstructure mainly composed by ferrite, acicular ferrite, bainite, tempered martensite, and martensite.
4. The tensile and bending tests showed both the changes in microstructure and the hardness inside the weld, leading to an increase of the mechanical properties within the welding zone, which results in failure outside the welding area.
5. The two-pass welding procedure has contributed to reaching a low dissimilar material mixture inside the weld, which can probably guarantee a better corrosion resistance of the clad material.

**Acknowledgments** The authors gratefully acknowledge the support given by the following laboratories: Physical Metallurgical Laboratory (LAMEF) in Brazil and Helmholtz Zentrum Geesthacht in Germany. Also, the authors would like to thank the financial support given by the National Council for Research and Development (CNPq), Shell Brasil

Petróleo Ltda, and National Agency of Petroleum, Natural Gas and Biofuel (ANP Commitment to investment in Research and Development). BK acknowledges financial support from DAAD via funds of the Federal Ministry of Education and Research (BMBF) under project number 57446973. RML received support from CNPq via project number 205724/2017 5, and CRdLL received financial support of CAPES PROBRAL 88881.198810/2018 01.

## References

- DuPont JN, Lippold JC, Kiser SD (2009) Welding metallurgy and weldability of nickel base alloys. John Wiley & Sons Inc, Hoboken, NJ
- Song KH, Nakata K (2010) Effect of precipitation on post heat treated Inconel 625 alloy after friction stir welding. *Mater Des* 31: 2942–2947. <https://doi.org/10.1016/j.matdes.2009.12.020>
- Rodriguez J, Ramirez AJ (2015) Microstructural characterisation of friction stir welding joints of mild steel to Ni based alloy 625. *Mater Charact* 110:126–135. <https://doi.org/10.1016/j.matchar.2015.10.023>
- Silva CC, Afonso CRM, Ramirez AJ, Motta MF, Miranda HC, Farias JP (2016) Assessment of microstructure of alloy Inconel 686 dissimilar weld claddings. *J Alloys Compd* 684:628–642. <https://doi.org/10.1016/j.jallcom.2016.05.231>
- Lloyd AC, Noël JJ, McIntyre S, Shoesmith DW (2004) Cr, Mo and W alloying additions in Ni and their effect on passivity. *Electrochim Acta* 49:3015–3027. <https://doi.org/10.1016/j.electacta.2004.01.061>
- Xu LY, Jing HY, Han YD (2018) Effect of welding on the corrosion behavior of X65/Inconel 625 in simulated solution. *Weld World* 62:363–375. <https://doi.org/10.1007/s40194-018-0549-y>
- Lemos GVB, Hanke S, Dos Santos JF, Bergmann L, Reguly A, Strohaecker TR (2017) Progress in friction stir welding of Ni alloys. *Sci Technol Weld Join* 22:643–657. <https://doi.org/10.1080/13621718.2017.1288953>
- DNV OS F101 (2013) DNV OS F101: submarine pipeline systems. Det Nor Verit 367. doi: DNV OS F101
- Souza RF, Ruggieri C, Zhang Z (2016) A framework for fracture assessments of dissimilar girth welds in offshore pipelines under bending. *Eng Fract Mech* 163:66–88. <https://doi.org/10.1016/j.engfracmech.2016.06.011>
- Chong TVS, Kumar SB, Lai MO, Loh WL (2016) Effects of elevated temperatures on the mechanical properties of nickel based alloy clad pipelines girth welds. *Eng Fract Mech* 152:174–192. <https://doi.org/10.1016/j.engfracmech.2015.11.003>
- Sulaiman NS, Tan H (2014) Third party damages of offshore pipeline. *J Energy Challenges Mech* 1:1–6
- DNV (2003) Classification of ships/high speed. Light Craft and Surface Craft. Det Norske Veritas, Høvik, p 43
- Xu LY, Li M, Jing HY, Han YD (2013) Electrochemical behavior of corrosion resistance of X65/Inconel 625 welded joints. *Int J Electrochem Sci* 8:2069–2079
- Maltin CA, Galloway AM, Mweemba M (2014) Microstructural evolution of Inconel 625 and Inconel 686CPT weld metal for clad carbon steel linepipe joints: a comparator study: the effect of iron dilution on the elemental segregation of alloying elements in nickel based filler metals. *Metall Mater Trans A Phys Metall Mater Sci* 45: 3519–3532. <https://doi.org/10.1007/s11661-014-2308-z>
- Dutra JC, Silva RHG e, Marques C, Viviani AB (2016) A new approach for MIG/MAG cladding with Inconel 625. *Weld World* 60:1201–1209. <https://doi.org/10.1007/s40194-016-0371-3>
- Mortezaie A, Shamanian M (2014) An assessment of microstructure, mechanical properties and corrosion resistance of dissimilar welds between Inconel 718 and 310S austenitic stainless steel. *Int J Press Vessel Pip* 116:37–46. <https://doi.org/10.1016/j.ijpvp.2014.01.002>
- Anbarasan N, Jerome S, Arivazhagan N (2019) Argon and argon hydrogen shielding gas effects on the laves phase formation and corrosion behavior of Inconel 718 gas tungsten arc welds. *J Mater Process Technol* 263:374–384. <https://doi.org/10.1016/j.jmatprotec.2018.07.038>
- Petrzak P, Kowalski K, Blicharski M (2016) Analysis of phase transformations in Inconel 625 alloy during annealing. *Acta Phys Pol A* 130:1041–1044. <https://doi.org/10.12693/APhysPolA.130.1041>
- Mills WJ (1984) Effect of heat treatment on the tensile and fracture toughness behavior of alloy 718 weldments. *Weld J* 8:237–245
- Paventhan R, Lakshminarayanan PR, Balasubramanian V (2011) Prediction and optimization of friction welding parameters for joining aluminium alloy and stainless steel. *Trans Nonferrous Met Soc China (English Ed)* 21:1480–1485. [https://doi.org/10.1016/S1003-6326\(11\)60884-4](https://doi.org/10.1016/S1003-6326(11)60884-4)
- Liu X, Lan S, Ni J (2014) Analysis of process parameters effects on friction stir welding of dissimilar aluminum alloy to advanced high strength steel. *Mater Des* 59:50–62. <https://doi.org/10.1016/j.matdes.2014.02.003>
- Zheng Q, Feng X, Shen Y, Huang G, Zhao P (2017) Effect of plunge depth on microstructure and mechanical properties of FSW lap joint between aluminum alloy and nickel base alloy. *J Alloys Compd* 695:952–961. <https://doi.org/10.1016/j.jallcom.2016.10.213>
- Wu AP, Song ZH, Nakata K, Liao JS (2013) Defects and the properties of the dissimilar materials FSW joints of titanium alloy TC4 with aluminum alloy 6061. *Proc 1st Int Jt Symp Join Weld*:243–248. <https://doi.org/10.1533/978-1-78242-164-1.243>
- Kar A, Suwas S, Kailas SV (2018) Two pass friction stir welding of aluminum alloy to titanium alloy: a simultaneous improvement in mechanical properties. *Mater Sci Eng A* 733:199–210. <https://doi.org/10.1016/j.msea.2018.07.057>
- Kasai H, Morisada Y, Fujii H (2015) Dissimilar FSW of immiscible materials: steel/magnesium. *Mater Sci Eng A* 624:250–255. <https://doi.org/10.1016/j.msea.2014.11.060>
- Coelho RS, Kostka A, dos Santos JF, Kaysser Pyzalla A (2012) Friction stir dissimilar welding of aluminium alloy to high strength steels: mechanical properties and their relation to microstructure. *Mater Sci Eng A* 556:175–183. <https://doi.org/10.1016/j.msea.2012.06.076>
- Kundu S, Roy D, Bhola R, Bhattacharjee D, Mishra B, Chatterjee S (2013) Microstructure and tensile strength of friction stir welded joints between interstitial free steel and commercially pure aluminium. *Mater Des* 50:370–375. <https://doi.org/10.1016/j.matdes.2013.02.017>
- Guo L, Zheng H, Liu S et al (2016) Effect of heat treatment temperatures on microstructure and corrosion properties of Inconel 625 weld overlay deposited by PTIG. *Int J Electrochem Sci* 11:5507–5519. <https://doi.org/10.20964/2016.07.97>
- Zareie Rajani HR, Akbari Mousavi SAA, Madani Sani F (2013) Comparison of corrosion behavior between fusion cladded and explosive cladded Inconel 625/plain carbon steel bimetal plates. *Mater Des* 43:467–474. <https://doi.org/10.1016/j.matdes.2012.06.053>
- Banovic SW, DuPont JN, Marder AR (2002) Dilution and microsegregation in dissimilar metal welds between super austenitic stainless steel and nickel base alloys. *Sci Technol Weld Join* 7: 374–383. <https://doi.org/10.1179/136217102225006804>
- Da Cunha PHCP, Lemos GVB, Bergmann L et al (2019) Effect of welding speed on friction stir welds of GL E36 shipbuilding steel. *J Mater Res Technol* 8:1041–1051. <https://doi.org/10.1016/j.jmrt.2018.07.014>
- Lemos GVB, Farina AB, Martinazzi D, et al (2016) Efeito da Velocidade de Rotação da Ferramenta na Soldagem por Fricção e Mistura Mecânica da Liga Inconel 625. In: ABM (ed) 71<sup>o</sup>

Congresso Anual da ABM Internacional. Rio de Janeiro, pp 1387-1395

33. DIN EN ISO 4136:2011-05 (2013) Destructive tests on welds in metallic materials - Transverse tensile test
34. Kim JS, Lee HW (2016) Effect of welding heat input on microstructure and texture of Inconel 625 weld overlay studied using the electron backscatter diffraction method. *Metall Mater Trans A Phys Metall Mater Sci* 47:6109-6120. <https://doi.org/10.1007/s11661-016-3754-6>
35. Silva CC, de Albuquerque VHC, Miná EM, Moura EP, Tavares JMRS (2018) Mechanical properties and microstructural characterization of aged nickel based alloy 625 weld metal. *Metall Mater Trans A Phys Metall Mater Sci* 49:1653-1673. <https://doi.org/10.1007/s11661-018-4526-2>
36. Reynolds AP, Posada WTM, Deloach J (2003) Friction stir welding of DH 36 steel. *Sci Technol Weld Join* 8:455-460. <https://doi.org/10.1179/136217103225009125>
37. Sundararaman M, Mukhopadhyay P, Banerjee S (1997) Carbide precipitation in nickel base superalloys 718 and 625 and their effect on mechanical properties. *Miner Met Mater Soc*:367-378. [https://doi.org/10.7449/1997/superalloys\\_1997\\_367\\_378](https://doi.org/10.7449/1997/superalloys_1997_367_378)